Quasimolecular electron promotion beyond the $1s\sigma$ and $2p\pi$ channels in slow collisions of He^{2+} and He

L. Ph. H. Schmidt, M. Schöffler, C. Goihl, T. Jahnke, H. Schmidt-Böcking, and R. Dörner
Institut für Kernphysik, Goethe-Universität, 60438 Frankfurt am Main, Germany
(Received 14 August 2015; revised manuscript received 10 March 2016; published 2 November 2016)

The electron emission pattern of transfer ionization in collisions of He^{2+} with He was investigated for impact velocities between 0.53 a.u. and 0.77 a.u. (7 keV/u–15 keV/u) employing recoil-ion momentum spectroscopy. This process is known to be dominated by the promotion of the $2p\pi$ quasimolecular orbital into the continuum which results in banana-shaped areas of high electron momentum densities in the collision plane extending from the target to the projectile in velocity space. Asymmetries are explained by a coherent superposition of the $1s\sigma$ channel of quasimolecular promotion with the $2p\pi$ channel. Here we report on additional contributions from channels of higher angular momentum which emerge at the smaller impact velocities. They show up as highly structured electron emission patterns in the plane perpendicular to the direction of impact.

DOI: 10.1103/PhysRevA.94.052701

I. INTRODUCTION

The collision of an ion with an atom can lead to the ejection of one or more electrons from the target to the continuum. For fast collisions, where the velocity of the projectile is faster than the typical velocity of the bound electrons, distinct features in the electron momentum distributions [such as the electron capture to the continuum (ECC) and the binary encounter peak] occur and are well understood nowadays. In slow collisions a binary encounter between the projectile and an electron in the target atom typically cannot transfer sufficient energy to knock out the electron from its orbital. A first suggestion for a mechanism which can still lead to electron ejection in such slow collisions dates back to the 1980s: Olson [1] found in classical trajectory calculations continuum electrons stranded between the projectile and target ion where the attraction of the two nuclei is at balance. These so-called saddle-point electrons are emitted with approximately half of the projectile velocity in the direction of the ion impact.

This classical picture of an ionization process via promotion on the saddle point has then been confirmed and refined in quantum mechanical approaches. For example, close coupling calculations successfully describe the electron transfer for slow collisions [2]. To represent the electron wave function in such close coupling calculations, a basis set containing atomic wave functions centered at both nuclei can be used. At impact velocities much below 1 a.u. and especially for homonuclear collision systems it is, however, appropriate to combine the atomic states to a quasimolecular basis [3] and then use the close coupling approach to calculate transitions between these molecular states. This theoretical treatment was developed in the early 1960s (see, for example, [4]). An early experiment, which confirmed the validity of the quasimolecular treatment for slow He^{2+} on helium collisions, was published by Keever and Everhart [5].

We briefly describe the basic idea of the quasimolecular treatment for p-H collisions where it is very transparent: The electron wave function during the collision is described in a basis consisting of electronic states of $H_2{}^+$ which are continuously adapted to the changing positions of the nuclei. Within this basis the initial and final states where the electron is located at one or the other nucleus are superpositions of the two lowest molecular states $1s\sigma_g$ and $2p\sigma_u$. The notation of the molecular states refers to the limit of united atoms. The actual location of the electron depends on the phase between these states. Therefore, an electron transfer is simply induced by a phase shift between the gerade and ungerade molecular states which can emerge because the binding energies of these states differ at small internuclear distances.

When the projectile is passing the target the internuclear axis between both rotates rapidly. This rotation effectively couples the $2p\sigma_u$ and $2p\pi_u$ states. In the asymptote of large internuclear distances this leads to electrons excited to the $2p$ atomic state. In addition to this coupling by rotation the change of the internuclear distance causes a coupling between states of the same symmetry as $1s\sigma_g$ and $3s\sigma_g$ [6]. These radial couplings result from an inadequate electron momentum space representation of the dynamical problem by adiabatic states. The radial coupling gets larger if the electron is excited to higher molecular orbitals because the momentum spread of the wave function decreases with the excitation and gets small with respect to the error of the adiabatic description.

In contrast to the quasimolecular basis states the atomic wave functions can be easily adapted to the impact velocity, but these wave functions fail to give a good description of the effects appearing at the closest approach of the nuclei. To combine the advantages of a molecular basis and a two-center atomic basis the triple-center treatment was developed [7]. Winter and Lin [8] applied this method to the ionization channel of p-H collisions aiming to represent the electron momentum space of electrons emitted with low energy with respect to the saddle of the nuclear Coulomb potential, as well as the bound states with sufficient precision. Triple-center calculations are also available for He^{2+} on He collisions [9] but electron emission patterns have not been reported for this collision system.

A pertinent problem for describing electron emission to the continuum in a slow collision within any close coupling scheme is that the electrons reach the continuum by "climbing up a ladder" of infinitely many Rydberg states via radial couplings between these states. To avoid the explicit treatment of these radial couplings through the whole Rydberg series of molecular states the hidden crossing (HC) method [10–12]

uses molecular pseudostates which merge an infinite number of adiabatic molecular states of the same symmetry.

Two examples of such a series of single-electron states leading to the continuum are $1s\sigma_g, 3d\sigma_g, 5g_g, \cdots$ and $2p\pi_u, 4f\pi_u, 6h\pi_u, \cdots$. While the number of nodes of the wave functions in the direction of the internuclear axis increases by two from state to state, the number of nodes in the middle plane of the molecule remains unchanged and characterizes the HC channel. In the discussion of the experimental results we name the HC channels by the first state of the series in order to refer to the nodal structure at the middle plane of the quasimolecule (plane perpendicular to the internuclear axis). However, this does not mean that the system actually passed through this first state during its quasimolecular promotion or even that a description of a two-electron system by this single-electron molecular state is reasonable.

In the case of a collision system with more than one electron, as He^{2+} on He, the potential energy curves cannot simply be described as the sum of single-electron binding energies. While two independent $1s$ electrons can individually promote along the $2p\sigma_u$ potential energy curve and remain bound a correlated system of these electrons will reach the single-ionization continuum at small internuclear distances. Therefore (even in the case of elastic scattering) the correlated system jumps over an infinite number of hidden crossings between adiabatic molecular Rydberg states (see, for example, [13]). By using nonadiabatic states, which are adapted to the most probable evolution of the system, it is possible to adapt the molecular treatment using small basis sets to the electron transfer and excitation channels of many electron systems. Nevertheless, at small internuclear distances the adiabatic potential energy curves of $H_2{}^+$ and the diabatic two-electron molecular states are very different and any single-active-electron approach is inappropriate.

For internuclear distances increasing to infinity, however, the bound and the ionized electrons separate and the effect of electron correlation disappears. Therefore, even in many electron systems, most of the saddle-point promotion can be treaded within single-active-electron approach. Accordingly, several theoretical works treating $p + \mathrm{H}$ collisions [14–16] have been successfully used for the interpretation of experimental data of $p + \mathrm{He}$ collisions [17].

The HC method describes the contributions of several molecular symmetries to the total ionization cross section, but it is not capable of producing correct momentum distributions of the continuum electrons. This problem was solved by Schultz, Ovchinnikov, Macek and co-workers in 2014 by switching from the HC method to a regularized lattice (RL) representation of the electronic wave function [18] during the expansion of the system. This is done at an internuclear separation, which is much larger than the impact parameter. The method which describes the transfer ionization $^{\mathrm{proj.}}\mathrm{He}^{2+} + \mathrm{He} \rightarrow {}^{\mathrm{proj.}}\mathrm{He}^{+} + \mathrm{He}^{2+} + \mathrm{e}^{-}$ was abbreviated by $2e$HC-RLTDSE [19]. The RL calculations solving the time-dependent Schrödinger equation (TDSE) are done for only one active electron evolving within the screened two-center potential of the two nuclei. The nuclei move along straight line trajectories of a representative impact parameter with constant velocity. Because the relevant rotational couplings appear during the first stage of the calculation using the $2e$HC approach the resulting electron emission pattern still includes the features related to two active electrons and a coherent superposition of different nuclear trajectories representing a specific momentum transfer.

Schmidt *et al.* have shown [20] that the main features of the electron emission pattern of this reaction at impact energies higher than 10 keV/u can be explained by a superposition of the $1s\sigma_g$ and $2p\pi_u$ channels of quasimolecular promotion. Several other collision systems show similar behavior [17,21,22] because a rotational coupling of a single active electron cannot populate states of higher angular momentum from the initially populated states. For an extension of these quasimolecular features to higher impact energies see [23].

The key difference between the single ionization and the transfer ionization (TI) is that the participation of both electrons in TI makes it more likely to transfer an angular momentum of $2\hbar$ due to rotational coupling from the nuclear motion to the electronic state instead of only $1\hbar$ in a single-electron process. Recently Schmidt *et al.* reported [19] that the electron emission pattern of the reaction

$$\mathrm{He}^{2+} + \mathrm{He} \rightarrow \mathrm{He}^{+}(1s) + \mathrm{He}^{2+} + e^{-}$$

at 10 keV/u projectile energy shows the signatures of the $3d\delta_u$ and $2s\sigma_g$ channels. The superposition of these two channels leads to creation of free vortices in the wave function of the emitted electron. The vortices only show up if reactions with a specific nuclear momentum exchange are selected.

In this paper we give a more detailed and more complete discussion of the extended series of experiments reported in [19]. We present measurements at six impact energies between 7 keV/u and 15 keV/u. The datasets are subdivided into many regions of internuclear momentum exchange. Based on fitting procedures of the electron emission pattern in the plane perpendicular to the direction of impact we discover further and so-far hidden channels of quasimolecular electron promotion to the continuum.

II. EXPERIMENT

The experiment was performed using a Penning ion source at the Institut für Kernphysik of the Goethe-University Frankfurt. A $^4\mathrm{He}^{2+}$ beam was accelerated with voltages between 14 keV and 30 keV. A magnetic mass-to-charge ratio selection was sufficient to separate the He^{2+} ions from $H_2{}^+$. Before entering a reaction microscope [24] the beam was collimated to a diameter less than 0.5 mm and a divergence less than 0.5 mrad.

The He^{2+} ion beam was crossed at 90° with a supersonic helium gas jet. This supersonic helium beam was produced by expanding gas at 16 bar through a 30 µm nozzle into a vacuum of 0.02 mbar. The nozzle was cooled to 140 K. Due to the expansion the internal temperature of the gas dropped to about 100 mK. With two differentially pumped skimmers (with 0.3 mm aperture opening each) we cut out a narrow and internally cold helium beam which had a diameter of 1 mm at the interaction region with the ion beam. We used a double-stage differentially pumped gas jet beam dump to keep the backpressure inside the reaction chamber below 10^{-8} mbar while the local density of helium atoms within the gas beam corresponds to a pressure above 10^{-5}mbar.

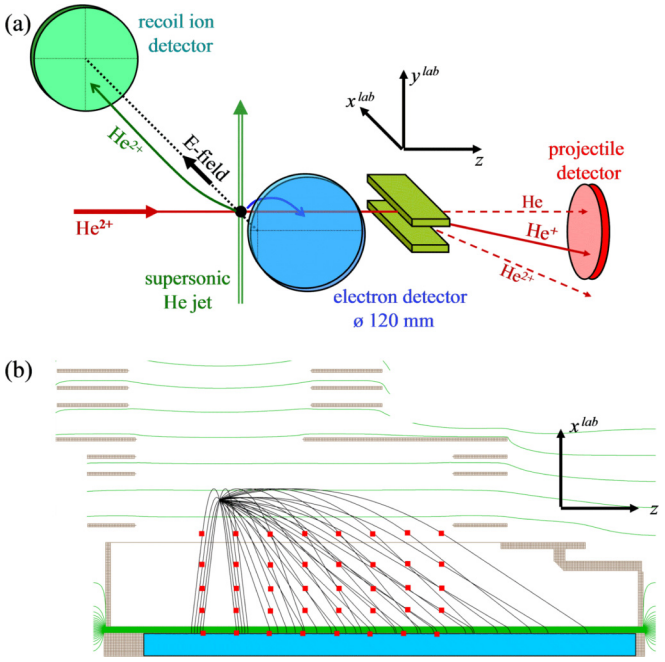

FIG. 1. Experimental setup: (a) Arrangement of the three detectors. (b) Simulated trajectories of electrons with momenta p_x = –0.2, –0.1, 0, 0.1, 0.2 a.u. and p_z = –0.05, 0.05, 0.15, ..., 0.65 a.u. The red squares show the electron positions 50 ns after the reaction time. The electrons with a momentum of 0.2 a.u. in the direction of the detector have already hit the detector.

After leaving the reaction region the projectile beam was charge-state selected by an electrostatic deflection scheme as sketched in Fig. 1(a). The projectiles which captured one or two electrons were detected by a microchannel plate detector (MCP) with delay line position readout [25] placed about 1.3 m behind the reaction region while the He^{2+} projectiles (that did not react with the target beam) were dumped in a Faraday cup. The projectile detector mainly provides the information on the charge state and gives a time reference for the time-of-flight measurements of the recoil ion and the electron. This time information has an uncertainty of about 1 ns caused by the projectile time of flight through the reaction region. This is the major limitation of the momentum spectroscopy of the emitted electron and the ionized target atoms which are detected in coincidence with the projectiles by using a reaction microscope [24].

The helium recoil ions and the electrons were extracted to opposite directions by a weak electric field of about 0.15 V/mm perpendicularly to the plane spanned by the two crossed beams [see Fig. 1(a)]. They were detected by two further position- and time-sensitive MCP detectors.

The electron arm of the momentum analyzer consists of an acceleration region of 13 mm length followed by a drift region of 26 mm separated by a mesh. After the drift the electrons are accelerated by a high field to the microchannel plate detector with a diameter of 124 mm. The center of this detector is shifted by 55 mm from the spectrometer axis in the direction of the projectile beam in order to spread the spatial distribution of electrons that occurs at velocities between zero and the projectile velocity over nearly the whole active surface of this detector [see Fig. 1(b)]. In the detector plane we achieved an electron momentum resolution of 0.01 a.u. mainly limited by the size of the reaction region of 1 mm (a.u. denotes atomic units: $m_e = e = \hbar = c/137 = 1$). In direction of the electric field the electron momentum was calculated from the time of flight resulting in a momentum resolution of about 0.02 a.u. [full width at half maximum (FWHM)], which mainly arises from the uncertainty of the timing reference obtained by the projectile detection.

The recoil ions passed through a system of electrostatic lenses and a drift region which minimizes the momentum uncertainty caused by the size of the reaction region. The electric field in the reaction region was optimized for the electron arm of the spectrometer which requires a homogeneous and very low field. This impacts the design of the recoil-ion arm: The recoil-ion distribution expands spatially to more than 40 mm before a first electrostatic lens can be placed. Therefore, a long recoil-ion drift region became necessary to achieve time-of-flight focusing yielding a total length of the recoil arm of about 1 m. Therein the ions' spatial distribution expands to 150 mm diameter perpendicular to the spectrometer axis before it can be refocused onto the detector of 80 mm diameter. The spectrometer voltage settings have been slightly changed between the measurements at different impact velocities. For all settings the recoil-ion momentum resolution was better than 0.2 a.u.

Both electron and recoil-ion momentum distributions are rotational symmetric with respect to the direction of the incoming beam which defines the z axis of our coordinate system. These symmetries can be used to adjust the calibration factors and offsets in the transverse plane.

The projectile scattering angle is inferred from the measured momenta of the recoil ion and electron using momentum conservation. Additionally, we measured the projectile scattering angle directly on the projectile detector but the corresponding projectile transversal momentum resolution is only about 5 a.u. (FWHM). Nevertheless, most of the background from statistical coincidences between projectiles and recoil ions can be eliminated by considering only those events which fulfill the momentum conservation within this resolution.

The recoil-ion momentum in the direction of the impact $p_{z,rec}$ is not continuously distributed because it is determined by momentum conservation in the z direction and by energy conservation. We used the measured $p_{z,rec}$ to determine the final-state binding energy of the He^+ and to once more reduce the statistical background by testing for energy conservation [26]. In the data analysis we consider only those events where the electron was captured into the $1s$ state of the projectile ion.

III. RESULTS AND DISCUSSION

In order to eliminate the laboratory frame rotation symmetries, we present the electron emission pattern in a frame of reference which is defined by the nuclear scattering plane. Because electron momentum components in the transverse plane are negligible compared to the nuclear momentum exchange, we simply use the transversal recoil-ion momentum and the direction of impact to define the nuclear scattering plane (x, z). The projection of the three-dimensional electron distributions onto the scattering plane is named "top view."

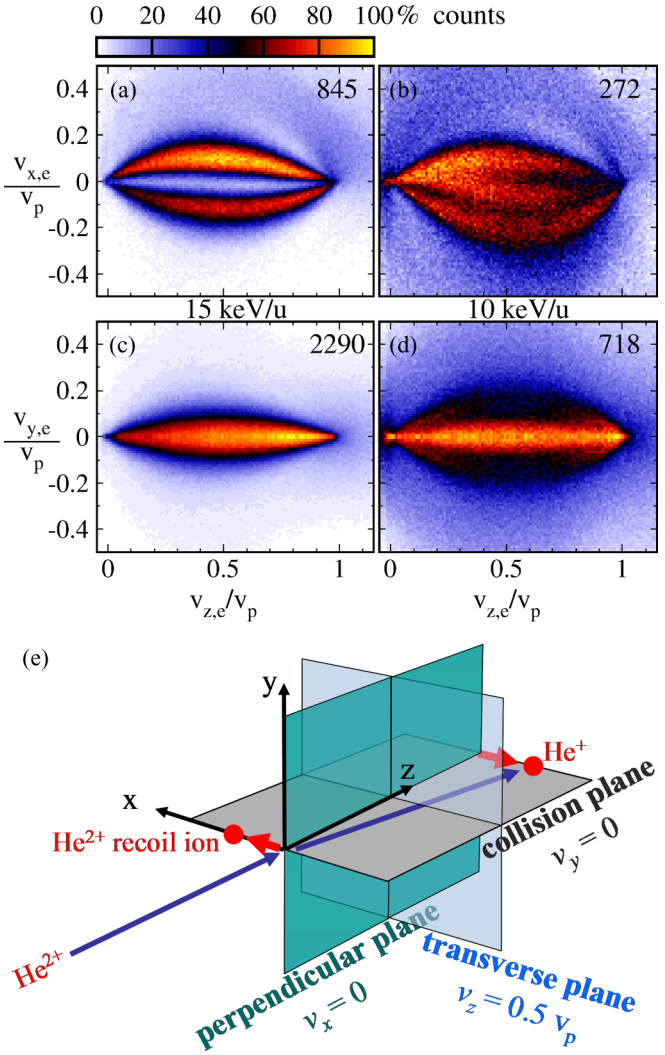

FIG. 2. Electron velocity distribution of the reaction $He^{2+} + He(1s^2) \rightarrow He^+(1s) + He^{2+} + e^-$ in units of the laboratory frame projectile velocity v_p. (a,b) are projections to the nuclear scattering plane (top view). (c,d) are projections to the perpendicular plane (side view). The number of measured events per bin (0.01×0.01) is given as a linear color scale with 50 colors. Each color represents a range of 2% of the maximum number of counts shown at the upper right of each panel. (a,c) are measured at 15 keV/u projectile energy and contain only events with small nuclear momentum exchange $p_{r,rec} = 1$ to 4 a.u. (b,d) show the equivalent distributions at 10 keV/u and higher nuclear momentum exchange of $p_{r,rec} = 10$ to 15 a.u. (e) depicts the geometric definition of the planes.

A second type of presentation used in many publications is the so-called "side view" where the electron distribution is projected to the perpendicular plane, which is defined by the vector perpendicular to the scattering plane (y axis) and the direction of impact (z axis). Figure 2(e) illustrates these planes.

We start the presentation of the results with selected examples of two-dimensional electron distributions in the two planes containing the direction of impact shown in Figs. 2 and 3. The purpose of these figures is to show why the plane perpendicular to the direction of impact needs to be investigated to give a complete overview of all our results.

For the highest measured impact velocity $v_p = 0.775$ a.u. (laboratory frame projectile energy = 15 keV/u) the electron emission pattern mainly consists of two crescent-shaped (or banana-shaped) areas of similar intensity centered in the scattering plane [Figs. 2(a) and 2(c)]. These areas extend from the velocity space location of the target nucleus to the projectile nucleus velocity. In the top view presentation shown in Fig. 2(a) the recoil-ion momentum points upwards and the projectile is scattered downwards. Atomic units ($e = m_e = \hbar = 1$) are used and therefore electron velocities and momenta are identical. We use electron velocities because the electron emission pattern is dominantly determined by the location of the nuclei in velocity space.

The velocity of the initial state of the target defines the origin of the coordinate frame. Electron velocities are scaled by the initial projectile velocity v_p. Therefore the outgoing projectile is approximately found at $(x,y,z) = (0,0,1)$. The change of both projectile and target nuclear velocities during the collision is below 1% and not visible on the scale of Fig. 2.

The two-banana structure in Fig. 2(a) is the signature of a molecular promotion dominated by the $2p\pi_u$ channel. The symmetry of the collision system enforces the dipole lobes of the π states to be oriented in the scattering plane. In the side view presentation shown in Fig. 2(c) the two bananas lie on top of each other which results in a single narrow distribution. Because there is no observable which could be used to define the direction of the y axis the electron distribution has to be symmetric with respect to the scattering plane ($y = 0$). We have confirmed that our data are mirror symmetric with respect to the operation $y \rightarrow -y$ and then added the counts in both regions in order to reduce the statistical error.

The measured double-banana structure emerges from a long series of quasimolecular transitions. The first step of this ladder is the promotion to the $2p\pi_u$ orbital. The further evolution of this distribution all the way to the continuum is similar to what one obtains from those classical trajectory calculations which motivated the concept of the saddle-point promotion: Those electrons which reach the middle plane of the quasimolecule at small internuclear distance and fail to follow one of the nuclei will be ionized. But as soon as they get out of the middle plane of the quasimolecule they will be focused to one of the nuclei by the attractive nuclear Coulomb potential. The RLTDSE calculations showed that with this focusing the number of nodes in the transverse plane is conserved but the original $2p\pi_u$ distribution is stretched to become the double-banana structure.

By slightly decreasing the impact energy the single differential cross section $d\sigma/dp_{r,rec}$ significantly shifts to a larger nuclear momentum exchange [20]. This effect is much stronger than one might expect from the small increment of the collision time. As a second example we selected a smaller projectile energy of 10 keV/u and a momentum range $p_{r,rec} = 10$ to 15 a.u. The top and side view spectra shown in Figs. 2(b) and 2(d) show a structure with more distinct features than the simple double-banana shapes resulting from the $2p\pi_u$ quasimolecular promotion. To unravel the channels and intermediate quasimolecular orbitals which give rise to these structures, we switch to a more differential presentation of the data: While in Fig. 2 the data have been integrated over the velocity space dimension which is not shown, we now select a

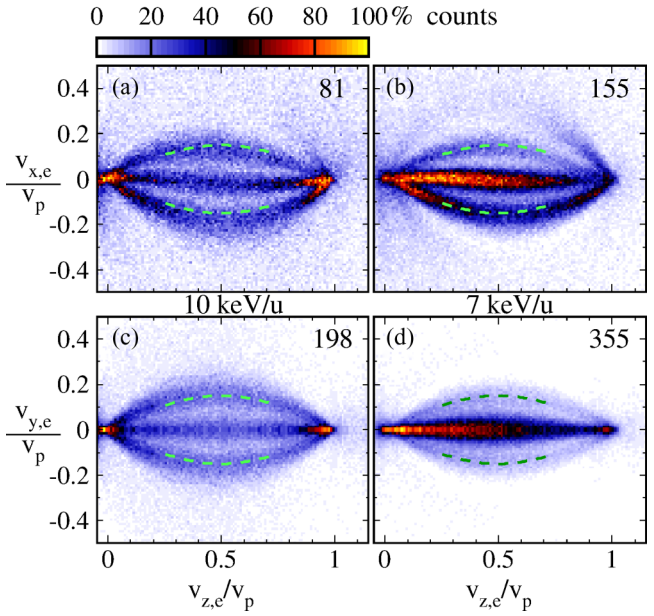

FIG. 3. Slices of the electron velocity distribution within the scattering plane (a,b) and the perpendicular plane (c,d): Only events with an out-of-plane velocity smaller than 0.04 v_p are shown. For both impact energies 10 keV/u (a,c) and 7 keV/u (b,d) a range of transversal recoil momenta $p_{r,rec} = 10$ to 15 a.u. is selected. The maximum number of counts (i.e., 100% of the color scale) is given at the upper right of each panel. The top and side view presentations corresponding to (a,c) are shown in Figs. 2(b) and 2(d).

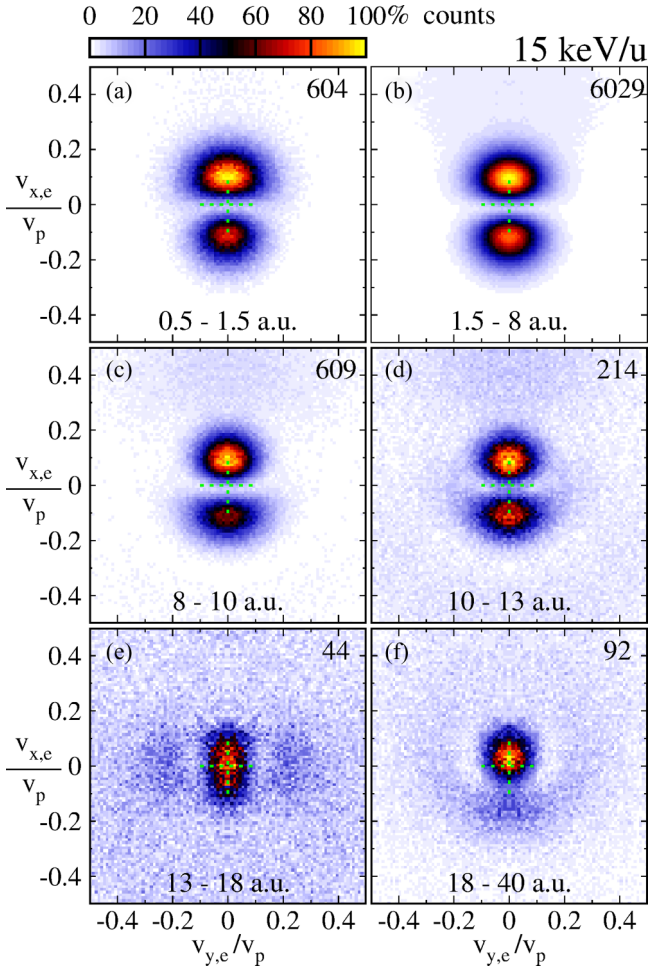

FIG. 4. Scaled electron velocity distribution within the plane perpendicular to the direction of impact for an impact energy of 15 keV/u (projectile velocity $v_p = 0.77$ a.u.) for different regions of recoil momentum transfer $p_{r,rec}$ as stated at the bottom of each panel. The measured velocities have been divided by $\sin(\pi v_{z,e}/v_p)$ before integrating in the beam direction from $v_{z,e} = 0.25\ v_p$ to $0.75\ v_p$. The transversal momentum transfer to the recoil ion defines the x axis; therefore the projectile is scattered downwards. The number of measured events is represented by a linear color scale with the maximum number of counts given at the upper right of each panel. The data are mirrored with respect to the scattering plane ($v_{y,e} = 0$) in order to reduce the statistical error. For nuclear momentum transfers above 12 a.u. the recoil-ion spectrometer does not have a full solid angle of detection.

subset of the dataset for which the momentum component out of the plane is very small ($\leqslant 0.04\ v_p$). Figures 3(a) and 3(c) show such slices. Surprisingly, we find similar structures in both planes consisting of three stripes with the outer stripes shaped like the double bananas. A further reduction of the projectile impact energy from 10 keV/u to 7 keV/u affects the structure in the scattering plane only marginally. But in the perpendicular plane the structure contracts to a single line, comparable to the side view structure observed at 15 keV/u.

Figure 3 shows that the stripes seen in both planes are approximately bent according to the function $C \sin(\pi v_z/v_p)$ which is shown as green dashed lines. We used $C = \pm 0.15$ in all panels of Fig. 3. For 7 keV/u the distributions show a significant asymmetry with respect to the middle plane defined by $v_{z,e}/v_p = 0.5$. Within the model of quasimolecular promotions such asymmetries indicate contributions of HC channels consisting of states with odd symmetry with respect to the middle plane of the quasimolecule as $3d\pi_g$ [19]. For simplification of the further discussions we focus on this middle plane where those states do not contribute. As a technical detail we mention that for analyzing the electron emission pattern in the transverse middle plane [light blue plane in Fig. 2(b)] we have to integrate over a broad range of v_z in order to have sufficient statistics to subdivide our datasets into many regions of nuclear momentum transfer. We included events with $0.25 < v_{z,e}/v_p < 0.75$. In this region of Fig. 3 we plotted the sine function. At both ends of the integration region the transversal electron distribution (x, y) has shrunken to about 71% of its size in the middle plane. To not obscure the structure by the z integration we scale the x and y components of the electron velocity by $1/\sin(\pi v_{z,e}/v_p)$ before integrating over $0.25 < v_{z,e}/v_p < 0.75$. The resulting transverse plane distributions of all six measured projectile energies are shown in Figs. 4–9.

A. Transverse plane electron emission pattern

Figure 4 shows the transverse plane electron emission pattern of the measurement at the highest projectile energy of 15 keV/u. The related top view and side view spectra at this energy for small $p_{r,rec}$ are shown in Figs. 2(a) and 2(c). The structure of the $2p\pi_u$ HC channel dominating at transversal recoil momenta $p_{r,rec}$ up to 13 a.u. shows up as two peaks

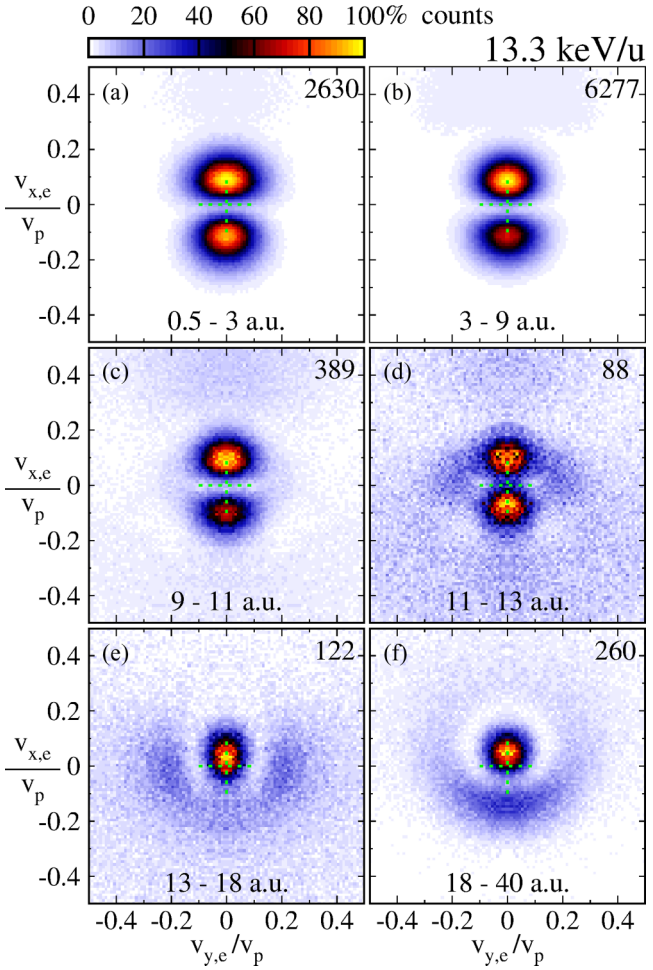

FIG. 5. Scaled electron transverse plane velocity distributions similar to Fig. 4 but for a smaller impact energy of 13.3 keV/u ($v_p = 0.73$ a.u.)

and resembles a textbook example of a dipole distribution. The dipole axis is vertical, which is the direction of nuclear momentum exchange. The spectra differ from the dipolar shape only at high nuclear momentum transfer. The numbers located at the upper right of each panel correspond to the number of entries of the strongest bin of the spectrum (bin size 0.01 × 0.01 a.u.). From these values it can be seen that collisions of high nuclear momentum transfer only give a minor contribution to the total cross section. This is why these non-$2p\pi_u$ contributions so far have not been resolved in earlier measurements with less resolution and statistics [20]. The two spots at positive and negative $v_{x,e}$ do not have exactly the same intensity. This results from an additional contribution of the $1s\sigma_g$ channel of quasimolecular promotion which adds up coherently to the $2p\pi_u$ peaks and therefore increases one of the spots while the other's intensity is reduced [21].

Next we show a representative sample of recoil-ion transversal momentum regions $p_{r,rec}$ from our comprehensive dataset. A more detailed presentation of the data can be found in the Supplemental Material [27]. By visual inspection of that dataset we have selected regions of $p_{r,rec}$ in which the electron emission pattern is rather constant and then integrated over $p_{r,rec}$ to improve the statistics. This yielded to the typical and representative pattern shown in Figs. 4–9.

The contributions of quasimolecular promotion beyond the $1s\sigma_g$ and $2p\pi_u$ channels become more visible when reducing the projectile energy. Figure 5 shows the results recorded at 13.3 keV/u, Fig. 6 those obtained at 11.5 keV/u, and Fig. 7 those for 10 keV/u projectile energy. For the case of the highest internuclear momentum exchange investigated we find a ring structure with a sharp spot at thecenter. Even though the structure is not exactly centered to the internuclear vector, we believe that it is caused by a quasimolecular promotion starting with the $2s\sigma_g$ state. The shift to positive values of x and the higher intensity at negative x which is seen in Figs. 5(f), 6(h), and 7(l) can be explained by a $2p\pi_u$ contribution, which is coherently added to the $2s\sigma_g$ channel.

B. Modeling of the experimental data by four channels of quasimolecular promotion

To the present day, a sophisticated theoretical description is only available for the emission pattern depicted in Fig. 7(i) which shows events with $p_{r,rec}$ of ∼12 a.u. for a projectile energy of 10 keV/u. As discussed in detail in [19] the structure observed is caused by the superposition of the $2s\sigma_g$ and $3d\delta_g$ channel. If the relative phase between the wave functions of these two channels is such that the cross term vanishes, then the four lobes of the $3d\delta_g$ channel fill up the ring-shaped node of the $2s\sigma_g$ channel. This happens for a relative phase of 90°.

Because the collision system is symmetric with respect to the scattering plane, two of the lobes have to be centered in the scattering plane which is plotted vertically with the recoil scattered upwards. The difference between the upper and the lower part is most probably caused by a small $2p\sigma_u$ contribution as mentioned above. At projectile energies of 12.5 keV/u and below several electron emission patterns can be assigned to such a superposition of the $3d\delta_g$, $2s\sigma_g$, and $2p\sigma_u$ HC channels [see, for example, Figs. 6(i), 8(g) and 9(h)].

In the following section we will investigate how much of the structures seen at the six projectile energies can be explained by restricting to the four quasimolecular channels we already identified and which have been described in [19]. Therefore we examine what variety of electron distributions $P(v_{e,x}, v_{e,y})$ can be obtained by superimposing only four two-dimensional (2D) model wave functions using complex coefficients c.

$$P(v_{e,x}, v_{e,y},) = |c_{1s\sigma}\psi_{1s\sigma} + c_{2p\pi}\psi_{2p\pi} + c_{2s\sigma}\psi_{2s\sigma} + c_{3d\delta}\psi_{3d\delta}|^2.$$

The model wave functions are constructed as $\psi(v_{r,e},\varphi) = R(v_{r,e})\cos(m\varphi)$. The azimuthal angle φ is related to Cartesian coordinates by $\varphi = \mathrm{atan}(v_{y,e}/v_{x,e})$ and $v_{r,e}^2 = v_{x,e}^2 + v_{y,e}^2$. The quantum number $m = 0, 1, 2$ describes the σ, π, and δ state. An accurate radial part of the velocity space wave function $R(v_{r,e})$ could be calculated by the RLTDSE method but for the present work we simply use model functions that fit best to the data. In Figs. 10(a)–10(d) we present the 2D densities of these model wave functions. The areas of high densities are labeled with the sign of the wave function which is real valued.

As an illustration Figs. 10(e) and 10(f) show two basic structures arising from only two of the model wave functions.

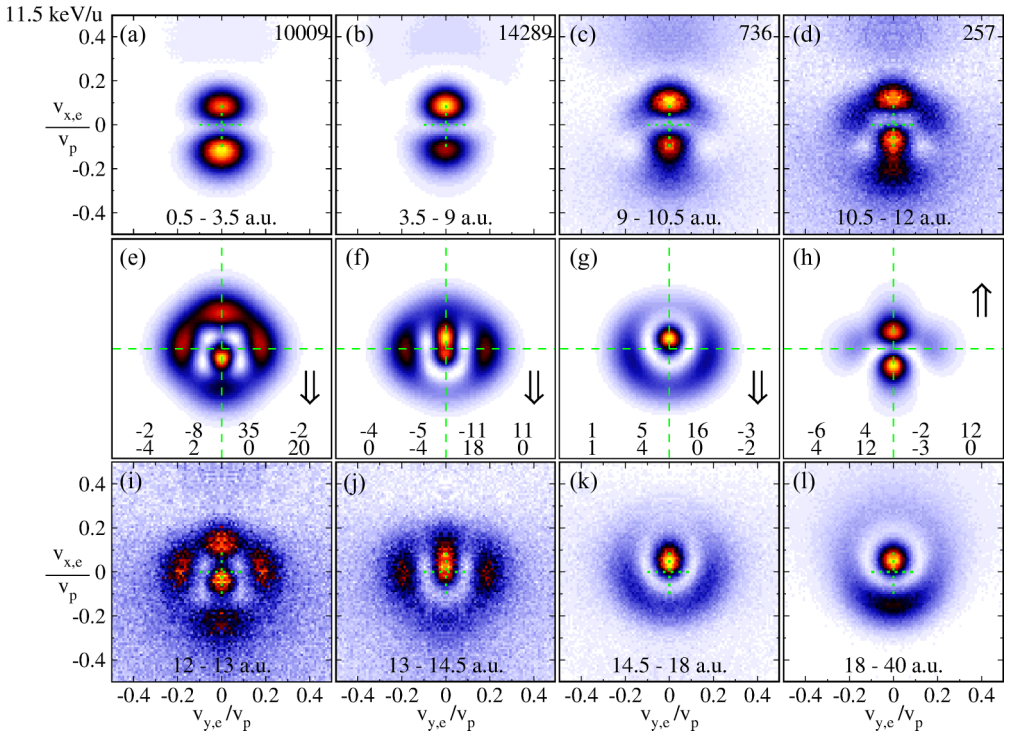

FIG. 6. Electron transverse plane velocity distributions. (a–d,i–l) Scaled experimental distributions recorded at a projectile energy of 11.5 keV/u (projectile velocity $v_p = 0.68$ a.u.). (e–h) Distributions modeled by the four states pictured in Figs. 10(a)–10(d). The real and imaginary part (upper and lower value, respectively) of the four coefficients of the $1s\sigma_g$, $2p\pi_u$, $2s\sigma_g$, and $3d\delta_g$ contributions are given in each panel.

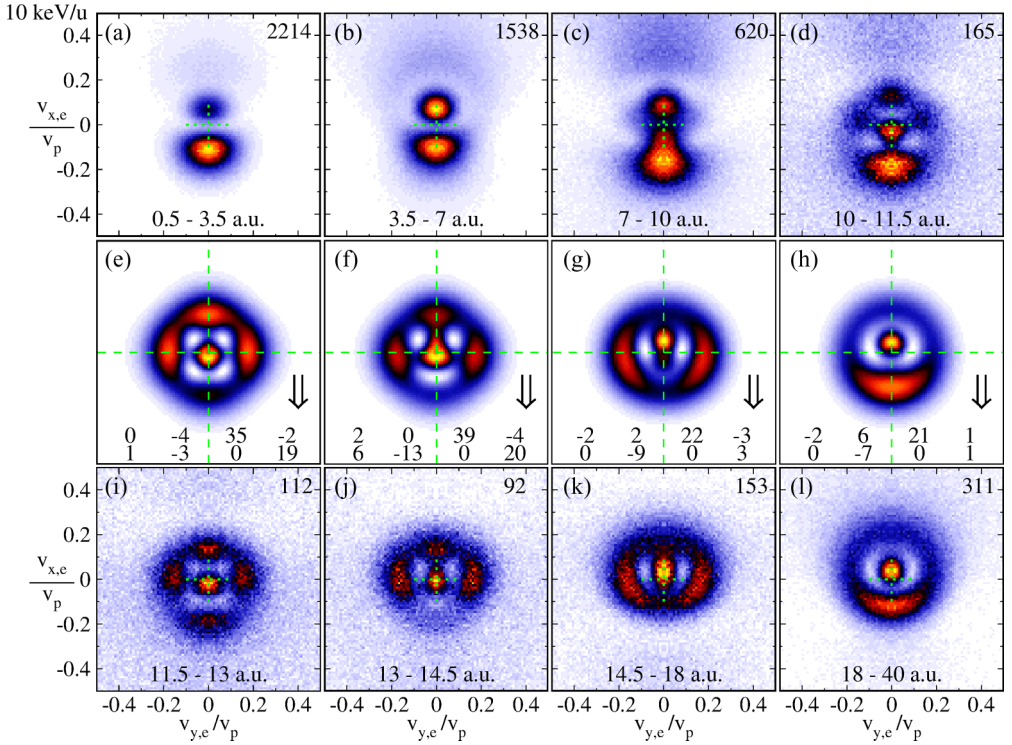

FIG. 7. Electron transverse plane velocity distributions. (a–d,i–l) Scaled experimental distributions measured at a projectile energy of 10 keV/u (projectile velocity $v_p = 0.63$ a.u.). (e–h) Distributions modeled by the four states pictured in Figs. 10(a)–10(d). The real and imaginary part (upper and lower values, respectively) of the four coefficients of the $1s\sigma_g$, $2p\pi_u$, $2s\sigma_g$, and $3d\delta_g$ contributions are given in each panel.

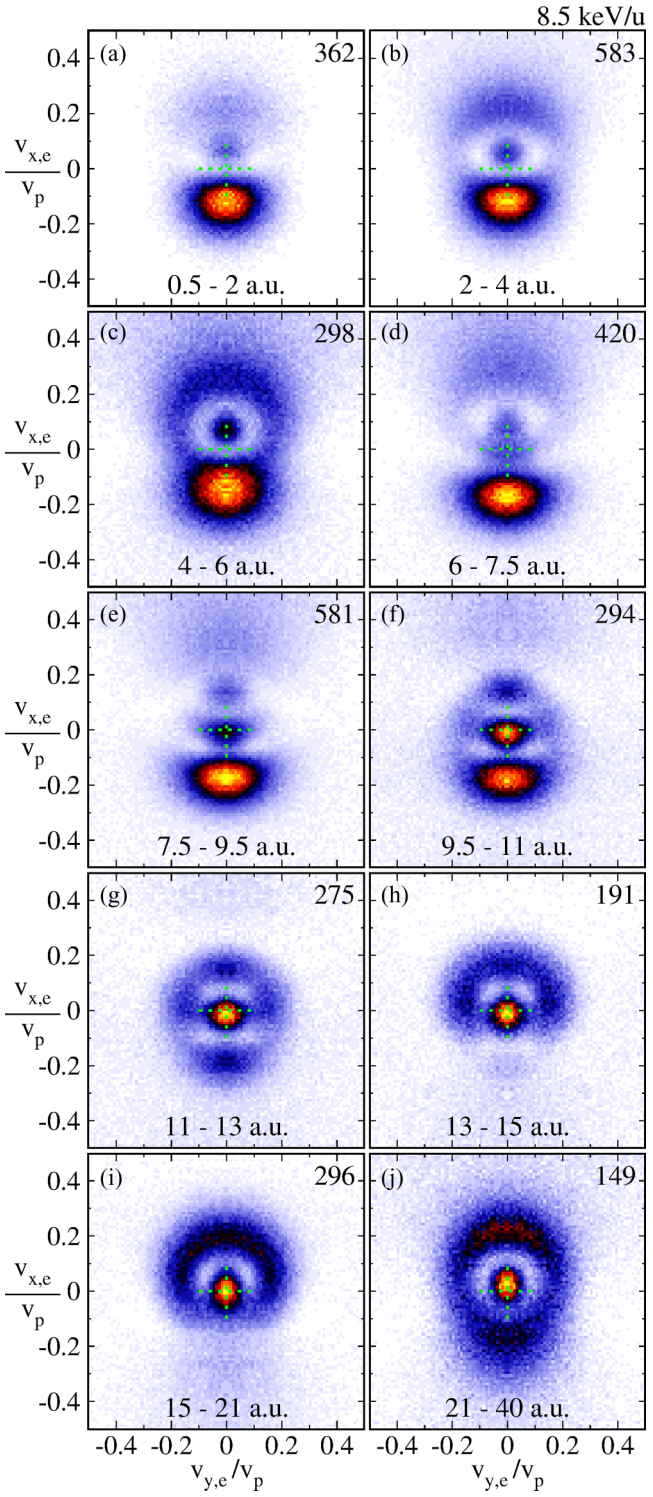

FIG. 8. Scaled electron transverse plane velocity distribution similar to Fig. 4 but for a smaller impact energy of 8.5 keV/u (projectile velocity $v_p = 0.58$ a.u.)

As mentioned above a slightly asymmetric dipole distribution as occurring in Fig. 10(e) results from the $2p\pi_u$ and $1s\sigma_g$ channel added with a relative phase of 0° or 180°. A phase difference of 90° would not lead to asymmetric peaks but cause a vanishing of the horizontal nodal line.

A superposition of the channels $2s\sigma_u$ and $3d\delta_g$ with approximately the identical magnitude and a phase difference of 90° is shown in Fig. 11(f). A remarkable aspect of this structure is the phase evolution close to the four local minima: On a circular path around each of these nodes the phase of the wave function changes by 360°. As described in detail in [19] this phase development is related to a quantum mechanical flux and therefore the experimental observation of this structure supports the theoretically predicted vortices occurring in the wave function of a single free electron.

Several of the experimental distributions can be modeled in surprising detail by superimposing the four quasimolecular channels. Figures 6(e)–6(h) and 7(e)–7(h) show a few examples of the modeled distributions. The arrows drawn inside these spectra point towards the corresponding experimental distributions. In each panel of these figures the real parts of the four coefficients are given in the upper line and the imaginary part in the lower line of values. The leftmost column belongs to the coefficient of the $1s\sigma_g$ channel followed by the $2p\pi_u$, $2s\sigma_g$, and $3d\delta_g$ coefficients. We adjusted the coefficients manually to best reproduce the measured data. Employing a numerical fitting procedure yielded much less satisfactory results—even with well adjusted start values of the fit parameters. This is probably due to the poor modeling of the radial part of the distribution. As we will later discuss in detail the number of fit parameters used here is too high to allow for an unambiguous determination of the parameters.

The major differences between the modeled and experimental distributions are contributions at the edges of the spectra (high $v_{r,e} = \sqrt{v_{x,e}^2 + v_{y,e}^2}$). These contributions are isotropic in many regimes of collision energy and nuclear momentum transfer. However, at internuclear momentum transfers between 3 a.u. and 10 a.u. we see a contribution directed towards the recoil side [upper part of the spectra; see, for example, Figs. 4(b), 5(b), 6(b), 7(c), 8(d), and 9(f)]. Similar contributions at the bottom of the spectra appear at higher internuclear momentum transfers and therefore can only be seen at the lower impact energies [Figs. 8(i) and 9(j)].

To visually enhance these contributions we present the corresponding subsets of the measurements at projectile energies of 7 keV/u and 8.5 keV/u as polar plots [Figs. 11(a)–11(d)]. These one-dimensional distributions can now be fitted using our model function for fixed $v_{e,r}$ employing standard fitting algorithms. We have either restricted our fit to only wave functions of σ, π, and δ symmetry ($m \leqslant 2$, blue lines) or we used φ states in addition ($m \leqslant 3$, red lines). Details of the fitting procedure are described in the Supplemental Material [27].

Over 500 fits of this type have been performed for all projectile energies, for small regions of transversal recoil momentum $p_{r,rec}$ and for small regions of $v_{r,e}$ with a width of 0.02 v_p. Figures 11(e) and 11(f) show two of these results in regimes where the δ symmetry dominates the angular distribution. The main result of the fitting is that within the experimental uncertainty we did not find any contribution of angular momenta higher than $m = 2$. The fitting results of $m \leqslant 3$ and $m \leqslant 2$ typically differ less than the statistical error of the measured data and the lines representing the fitting results can hardly be separated. Therefore, they are plotted

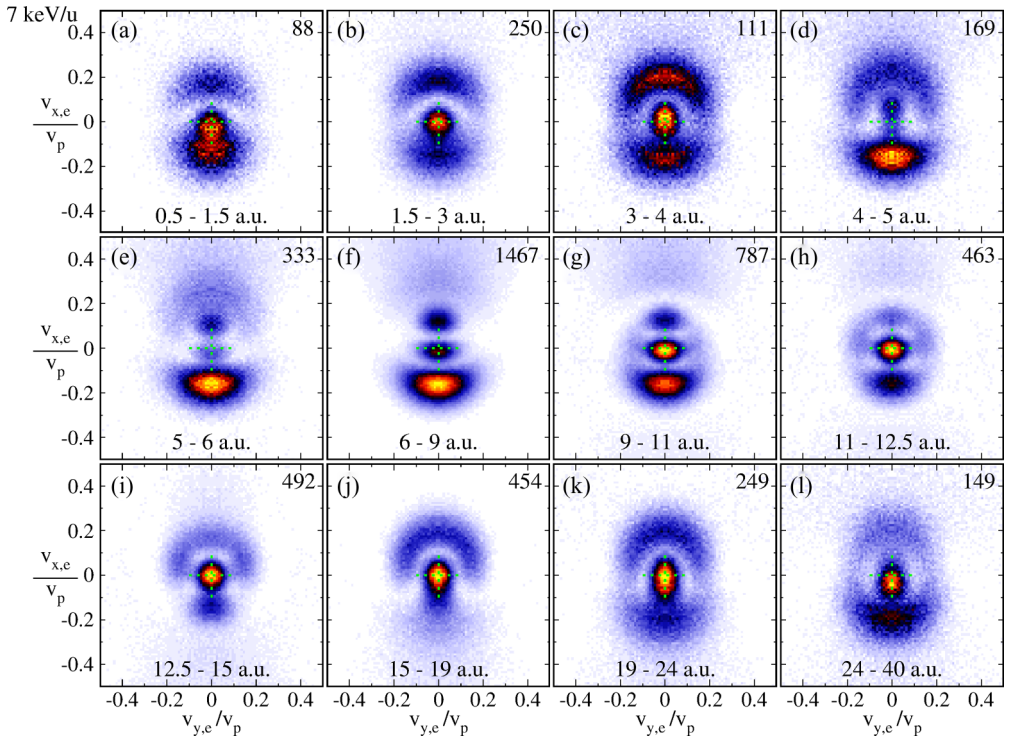

FIG. 9. Scaled electron transverse plane velocity distribution similar to Fig. 4 but for 7 keV/u projectile energy ($v_p = 0.53$ a.u.)

separately on the left and the right of the polar plots in Fig. 11. As mentioned above the experimental data have been mirrored in order to reduce the statistical errors.

C. Mechanism of electron promotion to the continuum

Before discussing the fitting results in detail we would like to speculate on the process which produces the outer loops on either the recoil or the projectile side. We will discuss this process within a single-active-electron model using H_2^+ states.

The initial state with the electron located at the target nucleus is described by a superposition of $1s\sigma_g$ and $2p\sigma_u$ states which are sketched in Figs. 12(a) and 12(d). During the approach of the nuclei on the incoming part of the collision trajectory $3d\sigma_g$ and $4f\sigma_u$ states can be populated by radial coupling. The population of further quasimolecular states by projectile target interactions starts to occur at internuclear distances of about 10 a.u. and reach a maximum strength at about 5 a.u. [28].

Depending on the representation of the electronic wave function radial couplings may appear up to infinite internuclear distances. These nonzero asymptotic couplings exist when using molecular states calculated within the adiabatic Born-Oppenheimer approach. They are not related to changes of projectile or target electronic state and appear because the used basis states are not suited for the description of the asymptotic region (see, for example, [29] and the references within). These artificial couplings are non-negligible at the collision energies of our investigation. However, while they increase with impact velocity, the interesting features of our experimental results become more prominent at lower impact velocities.

In any case, it can be assumed that when the internuclear vector starts to rotate rapidly not only the $1s\sigma_g$ and $2p\sigma_u$ states but the $3d\sigma_g$ and $4f\sigma_u$ states as well are populated, even though the electron was initially located in a $1s$ orbital of the target. Therefore these distributions are able to rotate into the transverse plane while the projectile passes the target as sketched in Figs. 12(c) and 12(f).

Due to couplings caused by the rotation of the internuclear axis not a pure quasimolecular state but a coherent superposition of several molecular states is populated. However, most simply one can expect the electric wave function (with some probability) to remain frozen in space while the nucleus passes by.

If the impact parameter is not too small the gerade and the ungerade channel (upper and lower part of Fig. 12) will stay in phase and therefore the electron is finally expected to be found at the recoil side where it was initially located. This was experimentally demonstrated in Figs. 11(a) and 11(b) where an intermediate nuclear momentum exchange was selected. Close collisions result in higher recoil transversal momenta and induce a phase shift between gerade and ungerade states because of their different binding energies at small internuclear distances. Therefore, the lobes which constructively added up move to the projectile side as shown in Figs. 11(c) and 11(d). We notice that it is not trivial to map this simple picture based on single-electron quasimolecular states to the correlation diagram of He_2^{2+} [3].

D. Amplitudes and phases of σ, π, and δ channels of HC promotion as a function of the radial electron momentum

Despite the success in modeling some of the electron distributions with only four basis states it is obvious that more quasimolecular states are needed. As mentioned above we can assume that only HC channels of σ, π, and δ

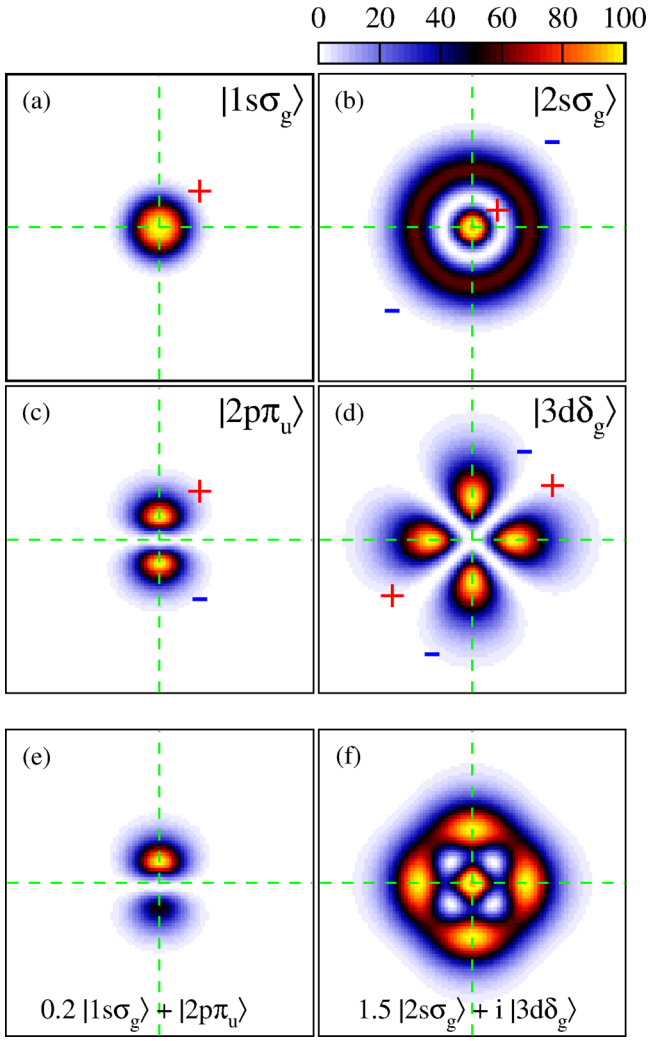

FIG. 10. Densities of the $1s\sigma_g$, $2p\pi_u$, $2p\sigma_g$, and $3d\delta_g$ contributions in the transverse plane which are used to model the measured spectra. The related wave functions are real valued. The radial component was adjusted by hand to best match the measured contributions. (e,f) show typical distributions which can be obtained by superimposing only two of these contributions.

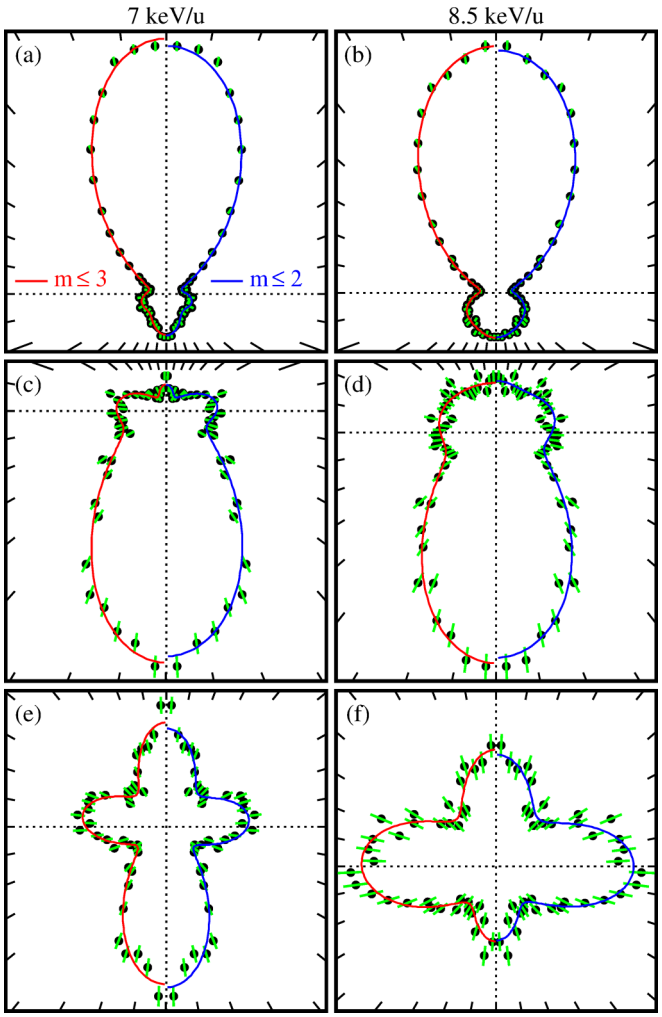

FIG. 11. Electron angular distributions in the transverse plane for 7 keV/u (a,c,d) and 8.5 keV/u (b,d,e) projectile energy in a polar representation. The momentum transfer to the recoiling ion points upwards. The experimental results (cycles with green error bars) contain events with (a,b) 6 a.u. $< p_{r,rec} <$ 8 a.u., 0.4 $v_p < v_{r,e} <$ 0.47 v_p [compare to Figs. 9(f) and 8(d)]. (c,d) 15 a.u. $< p_{r,rec} <$ 19 a.u., 0.4 $v_p < v_{r,e} <$ 0.47 v_p [compare to Figs. 9(j) and 8(i)]. (d,e) 11 a.u. $< p_{r,rec} <$ 12.5 a.u., 0.1 $v_p < v_{r,e} <$ 0.12 v_p [compare to Figs. 9(h) and 8(g)]. The data have been fitted under the assumption that quasimolecular channels with angular momentum up to $m = 3$ (red line, plotted at the left side of each plot) or only up to $m = 2$ (blue line, at the right) contribute [see Eq. (1)].

symmetry significantly contribute. To obtain the radial wave function of a specific angular momentum component we fit the electron angular distributions $P(\phi)$ in small regions of electron transversal velocities $v_{e,r}$ and recoil transversal momentum transfer $p_{r,rec}$.

For $\varphi = 0$ the electron is emitted in the direction of the recoil transversal momentum and $\varphi = \pm 90^\circ$ is perpendicular to the nuclear scattering plane. Only wave functions with an angular component of $\cos(m\varphi)$ contribute because the electronic system is symmetric with respect to the collision plane. We start our fitting procedure with angular momenta up to $m = 2$ and complex coefficients g_m:

$$P^m(\phi) = \left| \sum_{m=0,1,2} g_m \cos(m\varphi) \right|^2 . \quad (1)$$

We employed the program library MINUIT [30] to obtain values of g_m. Because the absolute phase of the wave function and the sign of the relative phases do not affect the measurable distribution this fitting does not provide a unique solution for the parameters. In addition to these trivial ambiguities of the phases, the absolute values of the contributions of σ (g_0), π(g_1), and δ(g_2) also show some ambiguities. The identity $2\cos^2(\varphi) = 1 + \cos(2\varphi)$ allows us to construct the probability distribution of a pure π state as the sum of an isotropic σ contribution and the cross term between σ and δ. However, because of the other cross terms between σ, π, and δ there are only two possible results for absolute values of the coefficients. Details of the fitting procedure are described in the Supplemental Material [27].

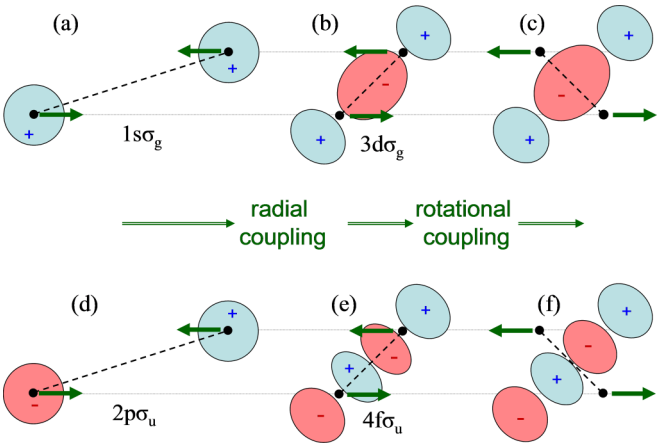

FIG. 12. Illustration of a population of high angular momentum quasimolecular states within a single-active-electron model. (a–c) show the case of an initial $1s\sigma_g$ quasimolecular orbital, (d–f) the corresponding process occurring for $2p\sigma_u$ states.

Figures 13(a), 13(c), and 14 show the absolute values of the coefficients $|g_0|$ (black lines), $|g_1|$ (red lines), and $|g_2|$ (green line). The sizes of the rectangles represent the uncertainties of the fit result. In most cases we obtained two results of contradictory meaning. They can be distinguished by the absolute value of the coefficient g_1 (π contribution) which enables us to obtain radial electron velocity depended functions $|g_m|(v_{r,e})$. These functions are the possible absolute values of the radial parts of the wave functions of the specific symmetry.

The absolute value of the δ amplitude $|g_2|$ is the same for both solutions. In case of small δ contribution the ambiguity of the σ and π contributions disappears as seen, for example, at the higher $v_{e,r}$ in Fig. 13(a).

The phases of the coefficients g_m cannot explicitly be determined but it is possible to arbitrarily select one of the possibilities at a specific $v_{e,r}$ and to connect the phases at the other values of $v_{e,r}$ under the assumption that the changes of g_m are minimal. Figure 13(b) shows the resulting curves for 10 keV/u projectile energy and recoil transversal momenta $p_{r,rec} = 5$ a.u. to 7 a.u. Here g_2 is chosen to be real valued for all $v_{r,e}$ but to avoid artificially strong phase changes of the σ and π contribution we have to allow negative values of g_2, which causes a phase jump of 180° at $v_{r,e} = 0.3\ v_p$ when the sign changes.

Obviously the phase related to the two possible absolute values of g_0 and g_1 have to differ to yield the same angular distributions. This is due to the cross terms between the σ, π, and δ distributions. The line types in Fig. 13 indicate which phase evolutions belong to which absolute values of the coefficients.

Figure 13(c) shows the results at $p_{r,rec} = 8$ a.u. to 11 a.u. Here the δ contribution shows only a very weak local minimum at those $v_{r,e}$ where Figs. 13(a) and 13(b) show the zero crossing. This indicates that the δ contribution consists of more than one HC channel. Thus the radial part of the wave function describing the sum of the δ contribution becomes a complex-valued function and it is not appropriate to fix the phase of g_2. When preprocessing the fitting results obtained at different

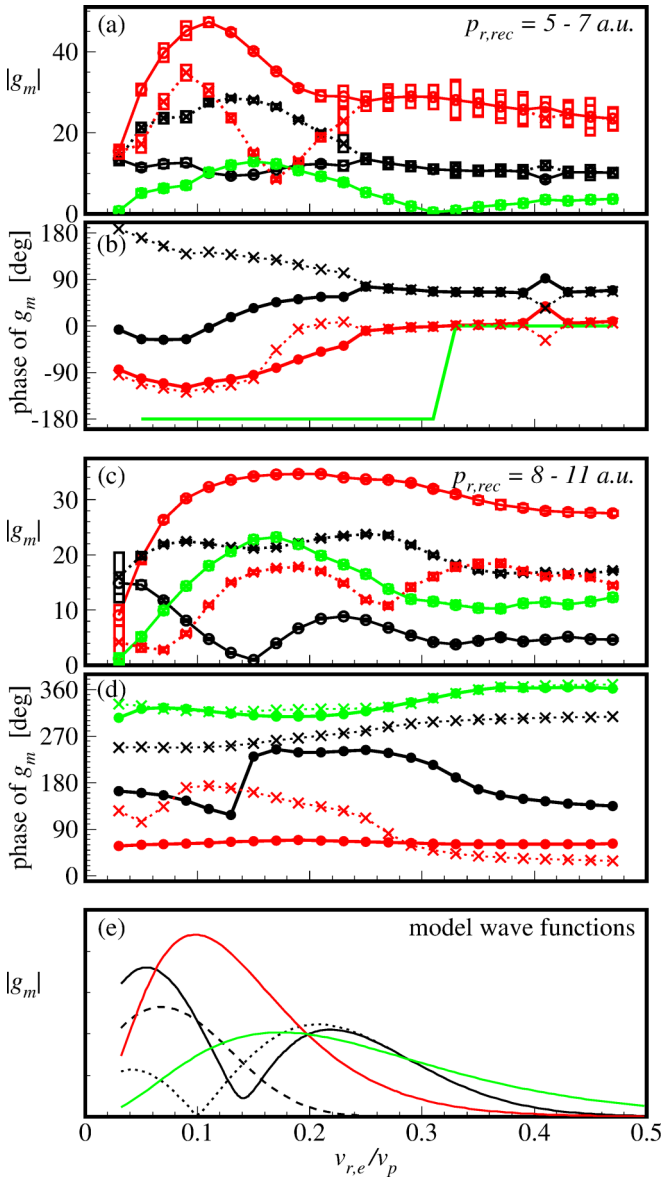

FIG. 13. Amplitudes of the σ (black, $m = 0$), π (red, $m = 1$), and δ (green, $m = 2$) contribution as a function of the electron transversal velocity $v_{e,r} = (v_{e,x}^2 + v_{e,y}^2)^{0.5}$ at 10 keV/u projectile energy. The experimentally determined absolute values $|g_m|$ of the coefficients are shown for recoil transversal momenta $p_{r,rec} =$ 5–7 a.u. (a) and $p_{r,rec} = 8$–11 a.u. (b). In most cases the fitting procedure provides two sets of g_m leading to identical angular distributions. The related phases of the g_m are shown in (b,d). The indeterminacy of the phases was reduced by minimizing the change of the coefficients with $v_{e,r}$. At $p_{r,rec} = 5$–7 a.u. (b) the δ contribution g_2 is restricted to real values. (e) Radial component of the wave functions visualized in Figs. 10(a)–10(d). Three σ states are shown as black lines: $1s\sigma$ (dashed line), $2s\sigma$ (dotted line), and a superposition of $1s\sigma$ and $2s\sigma$ with 30° relative phase (solid line).

$v_{r,e}$ to connect them to the curves shown in Fig. 13(d) we minimized the change of all three coefficients, g_0, g_1, and g_2.

The zero crossing of g_0 shown by the black solid lines in Figs. 13(c) and 13(d) can be assigned to the node of the radial wave function of the $2s\sigma_g$ channel. Results for the same region of $p_{r,rec}$ but different projectile velocities are shown in

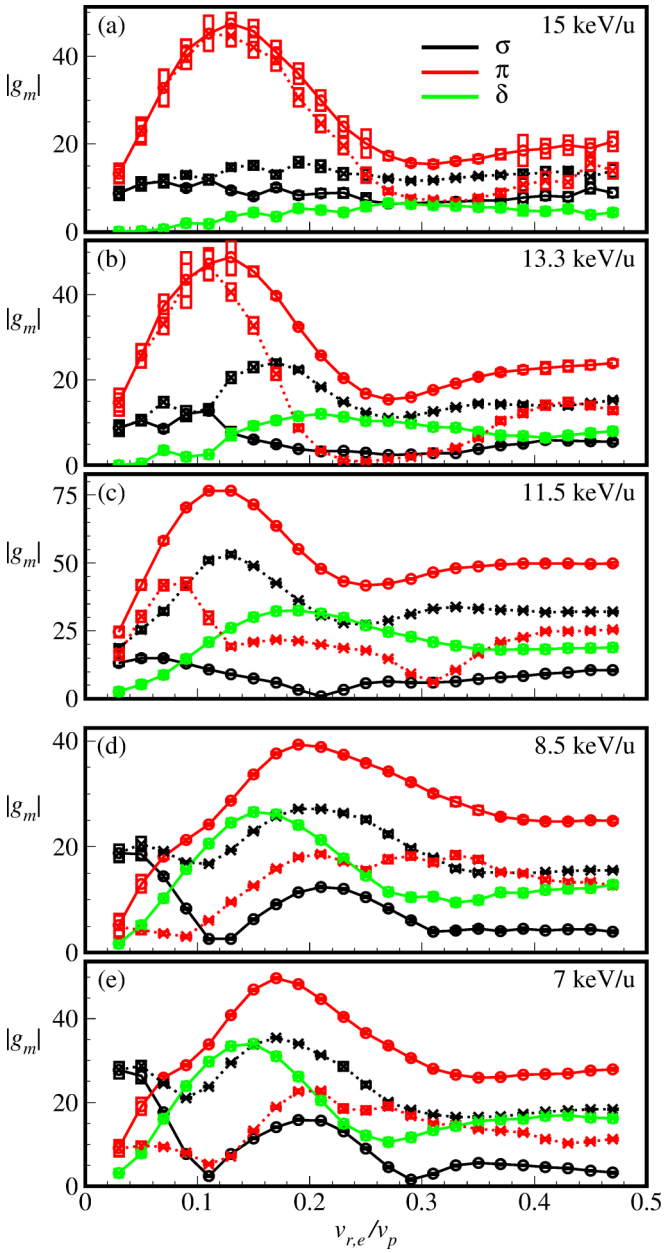

FIG. 14. Absolute values of the amplitudes of the σ (black), π (red), and δ (green) contribution as a function of the electron transversal velocity $v_{e,r} = (v_{e,x}^2 + v_{e,y}^2)^{0.5}$ at recoil-ion momenta $p_{r,rec} = 8$ a.u. to 11 a.u. for different projectile energies as labeled [the result at 10 keV/u is shown in Fig. 11(c)].

Fig. 14. The $v_{r,e}$ distributions of $|g_0|$ show minima at the lower projectile velocities. They are not fixed to a specific value of $v_{r,e}/v_p$ but change their position with increasing projectile energy to larger $v_{r,e}/v_p$. However, this does not suggest that the contribution of the $2s\sigma_g$ channel changes in that way. By adding the $1s\sigma_g$ channel coherently to the $2s\sigma_g$ channel the minimum of $|g_0|$ can be moved to a $v_{r,e}$ that is different from the position of the node of the pure $2s\sigma$ channel. Figure 13(e) visualizes the radial components of the two-dimensional model functions used in the previous section. The $1s\sigma_g$ and $2s\sigma_g$ parts are shown as dotted and dashed black lines. The solid black line shows the σ amplitude of a superposition of these channels. The minimum is slightly filled because the $1s\sigma_g$ and $2s\sigma_g$ channels have been added with a relative phase of 30°.

At the lowest projectile energies measured $|g|$ has a second local minimum at $v_{r,e} \approx 0.3\ v_p$ which is clearly visible in the fitting solution depicted by the solid lines but also present in the other solutions. A σ contribution with a second radial node suggests that not only $1s\sigma_g$ and $2s\sigma_g$, but also the $3s\sigma_g$ HC channel is relevant.

Figure 14 shows that the contribution of δ states strongly increases when the projectile energy is reduced from 15 keV/u to 7 keV/u. Contrarily, a corresponding increased production of $He^+(3d)$ by single-electron transfer is not predicted by close coupling calculations by Fritsch [2].

At 12.5 keV/u and 8 keV/u this calculation gives a cross section for the production of He^+ with $l = 3$ by electron transfer which is more than 5 times lower than the cross section of the $l = 2$ case. The magnetic quantum numbers of the states are not given but one can assume that the ratio of the total cross sections of $m = 3$ and $m = 2$ is much higher than the ratio between $l = 3$ and $l = 2$. This is consistent with our finding that HC channels of φ symmetry ($m = 3$) do not significantly contribute to the transfer ionization.

IV. SUMMARY

Since the mid-1990s hidden crossing theory had identified the so-called $1s\sigma_g$ and $2p\pi_u$ channels as the two main routes through which an electron is promoted to the continuum in a slow ion-atom collision. More recently the 2*e*HC-RLTDSE method [19] showed the existence of two more such routes to the continuum, the $2s\sigma_g$ and $3d\delta_g$ channels. The significantly increased statistics and improved resolution of the present experiment did lead to the discovery and identification of more channels. The importance of these additional channels rapidly increases at projectile energies below 10 keV ($v_p = 0.63$ a.u.). We identified the channels by fitting the electron distributions in the transverse middle plane of the quasimolecule and concluded that no angular momentum components higher than $m = 2$ are present. However, we found additional nodes in the radial component of the wave function of the three angular momentum contributions. Our fitting of amplitudes and phases, even though not completely unambiguous, will provide a benchmark test for future calculations which should include many more HC channels than the calculations presently available.

The experimental investigations using reaction microscopes easily provide the resolution to separate the electron transfer channels into different shells but only a few experiments provided sufficient energy resolution to determine the final-state angular momentum (e.g., [31]). Therefore, the measurement of the electron emission via the saddle-point process is a powerful alternative method to experimentally study the angular momentum transfer from the nuclear motion into the electronic system in slow ion-atom collisions.

Depending on the nuclear momentum exchange (i.e., the impact parameter) the occurrence of electrons with high radial velocity at either the recoil-ion side or the projectile side was observed at all projectile velocities. This points to a mechanism which leads to fixed relative phases between the contributions of different angular momenta. We suggest that this can be

explained by a radial coupling to higher quasimolecular states of σ symmetry while the projectile approaches followed by rotational coupling.

ACKNOWLEDGMENT

This work is supported by the Deutsche Forschungsgemeinschaft, http://gepris.dfg.de/gepris/projekt/136908543.

[1] R. E. Olson, Phys. Rev. A **27**, 1871 (1983).
[2] W. Fritsch, J. Phys. B **27**, 3461 (1994).
[3] C. H. Liu, J. G. Wang, and R. K. Janev, J. Phys. B. **45**, 235203 (2012).
[4] W. Lichten, Phys. Rev. **131**, 229 (1963).
[5] W. C. Keever and E. Everhart, Phys. Rev. **150**, 43 (1966).
[6] J. M. Rost, J. S. Briggs, and P. T. Greenland, J. Phys. B. **22**, L353 (1989).
[7] D. G. M. Anderson, M. J. Antal, and M. B. McElroy, J. Phys. B **7**, L118 (1974).
[8] T. G. Winter and C. D. Lin, Phys. Rev. A **29**, 567 (1984).
[9] J. Anton, B. Fricke, X. Ma, X. L. Zhu, B. Li, and H. P. Liu, Phys. Lett. A **369**, 85 (2007).
[10] E. A. Solov'ev, Phys. Rev. A **42**, 1331 (1990).
[11] S. Yu. Ovchinnikov, G. N. Ogurtsov, J. H. Macek, and Yu. S. Gordeev, Phys. Rep. **389**, 119 (2004).
[12] G. N. Ogurtsov, S. Yu. Ovchinnikov, J. H. Macek, and V. M. Mikoushkin, Phys. Rev. A **84**, 032706 (2011).
[13] F. Koike, H. Nakamura, S. Hara, Y. Itikawa, M. Matsuzawa, H. Sato, and I. Shimamura, J. Phys. B **11**, 4193 (1978).
[14] E. Y. Sidky and C. D. Lin, Phys. Rev. A **60**, 377 (1999).
[15] D. R. Schultz, C. O. Reinhold, P. S. Krstić, and M. R. Strayer, Phys. Rev. A **65**, 052722 (2002).
[16] J. H. Macek and S. Yu. Ovchinnikov. Phys. Rev. Lett. **80**, 2298 (1998).
[17] R. Dörner, H. Khemliche, M. H. Prior, C. L. Cocke, J. A. Gary, R. E. Olson, V. Mergel, J. Ullrich, and H. Schmidt-Böcking, Phys. Rev. Lett. **77**, 4520 (1996).
[18] T.-G. Lee, S. Yu. Ovchinnikov, J. Sternberg, V. Chupryna, D. R. Schultz, and J. H. Macek, Phys. Rev. A **76**, 050701 (2007).
[19] L. Ph. H. Schmidt, C. Goihl, D. Metz, H. Schmidt-Böcking, R. Dörner, S. Yu. Ovchinnikov, J. H. Macek, and D. R. Schultz, Phys. Rev. Lett. **112**, 083201 (2014).
[20] L. Ph. H. Schmidt, M. S. Schöffler, K. E. Stiebing, H. Schmidt-Böcking, R. Dörner, F. Afaneh, and T. Weber, Phys. Rev. A **76**, 012703 (2007).
[21] F. Afaneh, R. Dörner, L. Schmidt, Th. Weber, K. E. Stiebing, O. Jagutzki, and H. Schmidt-Böcking, J. Phys. B **35**, L229 (2002).
[22] M. A. Abdallah, C. L. Cocke, W. Wolff, H. Wolf, S. D. Kravis, M. Stöckli, and E. Kamber, Phys. Rev. Lett. **81**, 3627 (1998).
[23] R. T. Zhang, X. L. Zhu, W. T. Feng, D. L. Guo, Y. Gao, D. B. Qian, B Li, S. C. Yan, S. Xu, P. Zhang, and X. Ma, J. Phys. B. **48**, 144021 (2015).
[24] J. Ullrich, R. Moshammer, A. Dorn, R. Dörner, L. Ph. H. Schmidt, and H. Schmidt-Böcking, Rep. Prog. Phys. **66**, 1463 (2003).
[25] O. Jagutzki, A. Cerezo, A. Czasch, R. Dörner, M. Hattas, Min Huang, V. Mergel, U. Spillmann, K. Ullmann-Pfleger, T. Weber, H. Schmidt-Böcking, and G. D. W. Smith, IEEE Trans. Nucl. Sci. **49**, 2477 (2002).
[26] L. Ph. H. Schmidt, F. Afaneh, M. Schöffler, J. Titze, O. Jagutzki, Th. Weber, K. E. Stiebing, R. Dörner, and H. Schmidt-Böcking, Phys. Scr. T **110**, 379 (2004).
[27] See Supplemental Material at http://link.aps.org/supplemental/10.1103/PhysRevA.94.052701 for the comprehensive experimental dataset.
[28] D. S. F. Crothers and J. G. Hughes, Philos. Trans. R. Soc., A **292**, 539 (1979).
[29] A. K. Belyaev, Phys. Rev. A **82**, 060701(R) (2010).
[30] R. Brun, O. Couet, C. Vandoni, and P. Zanarini, *PAW Users Guide*, Program Library Q121, CERN, 1991.
[31] D. Fischer, B. Feuerstein, R. D. DuBois, R. Moshammer, J. R. Crespo López-Urrutia, I. Draganic, H. Lörch, A. N. Perumal, and J. Ullrich, J. Phys. B: At. Mol. Opt. Phys. **35**, 1369 (2002).